This is the accepted version of the work. The final published article is available at https://doi.org/10.1139/cgj-2019-0611

Reliability assessment of slopes with three-dimensional rotated transverse anisotropy in soil properties

L. Huang[1], Y.F. Leung[1]*

L. Huang, PhD candidate, Department of Civil and Environmental Engineering, The Hong Kong Polytechnic University, Hong Kong.

Email:16903778r@connect.polyu.hk

Y.F. Leung* (Corresponding author), Associate Professor, Department of Civil and Environmental Engineering, The Hong Kong Polytechnic University, Hong Kong.

Email: andy.yf.leung@polyu.edu.hk

Abstract: The influence of soil variability on three-dimensional (3D) probabilistic slope stability analysis has been previously investigated for soils that display isotropic spatial variability features or anisotropic horizontal fabric patterns. However, due to various soil deposition processes, weathering, filling or tectonic movements, the assumptions of isotropy or horizontal layering may not always be realistic. This study presents 3D analyses of slopes with spatially variable soils associated with rotated transverse anisotropy features. The results show that for cross-dip slopes where the strike direction of soil strata is perpendicular to the out-of-plane direction of the slope, the reliability depends on various factors including strata rotation angle and autocorrelation distances, and differs significantly from slopes with horizontally deposited soil fabric. The influence of strata orientation is also pronounced for dip slopes and reverse dip slopes, and these are presented in terms of reliability indices of the slopes and statistics of the length of sliding mass, and elaborated by considering the failure mechanism under different scenarios. Through these analyses, this paper discusses the key features of slope reliability considering rotated transverse anisotropy in soil properties, and their major differences in situations involving horizontal soil layers or two-dimensional probabilistic assessments.

Keywords: *Rotated transverse anisotropy; 3D probabilistic slope stability analyses; Soil spatial variability; Reliability index; Slide length.*

Introduction

Spatial variability in soil properties is a prominent source of uncertainty in slope reliability analysis. Through random field theory (Vanmarcke 1984), its effects on slope stability have been extensively investigated over the past few decades (Griffiths and Fenton 2004; Griffiths et al. 2009a; Cho 2010; Hicks and Spencer 2010; Huang et al. 2010; Wang et al. 2011; Jha and Ching 2013; Li et al. 2013; Jiang et al. 2014; Hicks et al. 2014; Jiang et al. 2015; Li et al. 2015a; Li and Chu 2015; Jiang and Huang 2016; Li et al. 2016; Lo and Leung 2017; Hicks and Li 2018; Liu et al. 2018; Lo and Leung 2018). While previous studies mainly focused on soils with isotropic or horizontally deposited fabric pattern, slopes with tilted stratifications are often observed in nature. For example, Zhu and Zhang (2013) discussed five typical patterns of spatial variability of rocks and soils (i.e. isotropy, horizontal transverse anisotropy, rotated transverse anisotropy, general anisotropy and general rotated anisotropy), and their combinations in various geological conditions. The influence of rotated transverse anisotropy in soil correlations has been discussed by Hicks and Onisiphorou (2005), who investigated the potential for liquefaction in a slope with spatially variable properties in two dimensions. Later, Griffiths et al. (2009b) studied the effects of rotated transverse anisotropy on the probability of 2D slope failure, where the autocorrelation distance in one direction was set to infinity. Later, Zhu et al. (2019) investigated the stability and failure mechanism of a slope using 2D random fields with rotated transverse anisotropy. Despite these previous works, the influence

of rotated transverse anisotropy on three-dimensional (3D) probabilistic slope stability analyses has not yet been investigated or reported in detail.

Horizontal transverse anisotropy (i.e. where soils display a horizontally deposited fabric pattern) has been considered in 3D probabilistic slope stability analyses in a number of studies (e.g., Hicks and Spencer 2010; Hicks et al. 2014; Li et al. 2015b; Hicks and Li 2018; Varkey et al. 2019). In general, three failure modes can be observed, depending on the ratio of the horizontal autocorrelation distance [i.e., major autocorrelation distance (θ_h)] to the slope length (L) and slope height (H): (a) when the ratio is small, e.g., $\theta_h < H$ as suggested by Hicks and Spencer (2010), the result is similar to conventional 2D deterministic analysis, and this is referred to as failure mode 1; (b) when the ratio falls within an intermediate range of $H < \theta_h < L/2$, discrete failure zones can be observed along the slope length, and this is known as failure mode 2; (c) when the ratio is large enough, e.g., $\theta_h > L/2$, the soil properties are similar at different locations along the horizontal directions, and this leads to failure mode 3, where the 3D probabilistic slope stability analysis tends to produce similar results to the 2D counterparts under plane strain conditions.

Assumptions of horizontal soil fabric pattern may not always be realistic since rotation of soil strata can result from various geological processes, leading to the rotated transverse anisotropy. In a three-dimensional model, this can be represented by the strike direction, dip direction and dip angle (Fig. 1). The relationship between orientations of soil stratigraphy and slope geometry is an important factor that can

affect slope stability. In practice, three scenarios are often encountered, as shown in Figs. 1(a), (b) and (c). The cross-dip slope (i.e., dip direction of strata is perpendicular to that of the slope) (Fig. 1(a)) and the reverse-dip slope (i.e., dip direction of strata is in the opposite direction to that of the slope) (Fig. 1(c)) are often considered as favorable scenarios for slope safety, whereas the dip slope (i.e., dip direction of strata is the same as that of the slope) (Fig. 1(b)) usually constitutes adverse conditions. These scenarios cannot be considered by assuming horizontally deposited soil strata. Besides, the findings regarding the three failure modes in 3D probabilistic slope stability analyses may be different when considering rotated transverse anisotropy, since the soil bedding planes are no longer in the horizontal orientation.

This study considers three categories of 3D rotated transverse anisotropy: (1) where the strike direction of strata is perpendicular to the out-of-plane direction of the slope ("rotated anisotropy around the x axis" as shown in Fig. 1(a)); (2) where the strike direction of strata is in the out-of-plane direction of the slope ("rotated anisotropy around the y axis" as shown in Figs. 1(b) and (c)); and (3) "rotated anisotropy around the z axis" as shown in Fig. 1(d). Compared to categories (1) and (2), category (3) may be less common, but can be found in saprolitic soils resulted from preferential weathering of rocks (Liu and Leung 2018). In this study, 3D slope stability analyses are presented with the soil idealized as a Tresca material. Effects of soil variability were investigated using the 3D random finite element method (RFEM), which combines the finite element method with random field modelling under the

Monte Carlo framework.

Methodology

Spatially correlated variables can be represented by the following linear equation that combines the fixed effect and the random effect:

$$\mathbf{z} = \boldsymbol{\mu} + \mathbf{e} \tag{1}$$

where $\mathbf{z}$ denotes the spatially variable soil properties at different locations, and the fixed effect and random effect are represented by the deterministic trend $\boldsymbol{\mu}$ and the residual $\mathbf{e}$, respectively. When a prevalent trend is not observed in the data, $\boldsymbol{\mu}$ is often assumed to be a constant mean vector, with $\mathbf{e}$ being the deviations from this mean (or trend). If the standard deviation σ is assumed to be constant for $\mathbf{z}$, the covariance matrix ($\mathbf{V}$) of the residual $\mathbf{e}$ can be factored as follows:

$$\mathbf{V} = \sigma^2 \mathbf{R} \tag{2}$$

where $\mathbf{R}$ is the spatial autocorrelation matrix. To avoid generating non-physical negative values, a log-normal distribution is often adopted for some soil properties, in which case the random field can be modeled through the following transformation:

$$\mathbf{z} = \exp(\mu_{\ln z} + \sigma_{\ln z}\boldsymbol{\varepsilon}) \tag{3}$$

where $\boldsymbol{\varepsilon}$ = vector of correlated random variables; $\mu_{\ln z}$ = mean of the logarithm of the soil property; $\sigma_{\ln z}$ = standard deviation of the logarithm of the soil property.

Many approaches, such as Cholesky decomposition, local average subdivision (Fenton and Vanmarcke 1990) and Karhunen-Loeve expansion (Li and Der Kiureghian 1993), etc., can be adopted to generate $\boldsymbol{\varepsilon}$ for the random field in Eq. (3). The Cholesky decomposition is adopted in the current study, with the property value of the random field assigned to each element based on the location of its midpoint. Through the Cholesky decomposition:

$$\mathbf{R} = \mathbf{L}\mathbf{L}^{\mathrm{T}} \tag{4a}$$

$$\boldsymbol{\varepsilon} = \mathbf{L}\mathbf{s} \tag{4b}$$

where $\mathbf{L}$ = Cholesky factor of $\mathbf{R}$; and $\mathbf{s}$ = vector of independent standard normal random variables.

The autocorrelation matrix $\mathbf{R}$ is formulated based on spatial variability features of the soil properties, which can be expressed mathematically by various forms of autocorrelation functions (single exponential function, squared exponential function, etc.). To incorporate rotated transverse anisotropy, the autocorrelation structure can be derived through rotation of the coordinate system (Zhu and Zhang 2013; Liu and Leung 2018). For instance, for rotated anisotropy around the x axis, the autocorrelation function is expressed as:

$$\rho = \exp\left[-2\sqrt{\frac{\Delta_x{}^2}{\theta_h{}^2} + \frac{\left(\Delta_y \cos\alpha + \Delta_z \sin\alpha\right)^2}{\theta_h{}^2} + \frac{\left(-\Delta_y \sin\alpha + \Delta_z \cos\alpha\right)^2}{\theta_v{}^2}}\right] \tag{5a}$$

For rotated anisotropy around the y axis, the autocorrelation function is given by:

$$\rho = \exp\left[-2\sqrt{\frac{(\Delta_x \cos\alpha + \Delta_z \sin\alpha)^2}{{\theta_h}^2} + \frac{{\Delta_y}^2}{{\theta_h}^2} + \frac{(-\Delta_x \sin\alpha + \Delta_z \cos\alpha)^2}{{\theta_v}^2}}\right] \quad \text{(5b)}$$

For rotated anisotropy around the z axis, the autocorrelation function is given by:

$$\rho = \exp\left[-2\sqrt{\frac{(\Delta_x \cos\alpha + \Delta_y \sin\alpha)^2}{{\theta_h}^2} + \frac{(-\Delta_x \sin\alpha + \Delta_y \cos\alpha)^2}{{\theta_v}^2} + \frac{{\Delta_z}^2}{{\theta_h}^2}}\right] \quad \text{(5c)}$$

In the above equations, Δ_x, Δ_y and Δ_z are separation distances between two locations in the x, y and z directions, respectively. θ_h denotes the major autocorrelation distance (i.e. two orthogonal directions in the bedding plane with one of them along the strike direction), and θ_v is the minor autocorrelation distance perpendicular to the bedding plane. α is the angle of rotation of the fabric pattern. Some typical realizations of random fields of rotation around the x and y axes are shown in Figs. 2 and 3, respectively.

With the autocorrelation structure determined by Eqs. (5a), (5b) or (5c), the autocorrelation matrix **R** can be formulated as follows:

$$\mathbf{R}_{n_e \times n_e} = \begin{vmatrix} 1 & \rho(\Delta_{x_{12}}, \Delta_{y_{12}}, \Delta_{z_{12}}) & \cdots & \rho(\Delta_{x_{1n_e}}, \Delta_{y_{1n_e}}, \Delta_{z_{1n_e}}) \\ \rho(\Delta_{x_{21}}, \Delta_{y_{21}}, \Delta_{z_{21}}) & 1 & \cdots & \rho(\Delta x_{2n_e}, \Delta y_{2n_e}, \Delta z_{2n_e}) \\ \vdots & \vdots & \ddots & \vdots \\ \rho(\Delta_{x_{n_e 1}}, \Delta_{y_{n_e 1}}, \Delta_{z_{n_e 1}}) & \rho(\Delta_{x_{n_e 2}}, \Delta_{y_{n_e 2}}, \Delta_{z_{n_e 2}}) & \cdots & 1 \end{vmatrix} \quad \text{(6)}$$

where n_e is the number of elements of the domain (e.g., finite element mesh), and the separation distances are those between the midpoints of two elements denoted by the

subscripts.

The current study adopts 3D RFEM to conduct probabilistic slope stability analyses. With the use of a commercial finite element software (i.e. ABAQUS), the RFEM is implemented in a non-intrusive manner, where the random fields are generated by MATLAB and then mapped onto the finite element model constructed using ABAQUS. For each parametric setting (i.e., α, θ_h, and L), 500 realizations are generated by the Monte Carlo approach with the Latin hypercube sampling technique, and then analyzed using the finite element method. The implementation procedure is summarized as follows:

Step 1: Construct the slope model using ABAQUS and define the input parameters of the random field (e.g., mean, standard deviation, probability distribution of soil properties, and autocorrelation structure).

Step 2: Formulate the autocorrelation matrix **R** using Eqs. (5a), (5b), and (5c).

Step 3: Generate 500 realizations of random fields using Eq. (3), and map the random fields onto the finite element mesh to construct 500 models with spatially variable soils.

Step 4: Conduct slope stability analysis for each of the 500 models and then evaluate the mean and standard deviation of the factor of safety (FS), reliability index (β) and the statistics of the length of the sliding mass (in the y-direction).

Illustrative example

Fig. 4(a) shows a cross-section of the 3D slope model. The slope has a height of 5 m and a slope angle of 45°. The base case involves a slope length (L) of 60 m, while various other slope lengths will also be considered later. As shown in Fig. 4(b), the finite element mesh with L = 60 m contains 9300 elements and the element size is 0.5 m × 0.5 m × 1 m (y-direction). Griffiths and Marquez (2007) suggested that a finer mesh would result in a smaller FS in the 3D finite element analysis of slopes, but the difference is usually small. Meanwhile, for random field generation, a smaller element size would lead to a more realistic simulation of spatially variable soils. Huang and Griffiths (2015) recommended that the element size in RFEM should be less than half of the spatial autocorrelation distance using an element-level averaging method. However, they also pointed out that only 2D random fields of undrained shear strength (c_u) were simulated in their studies, and the recommendations on element size could be different in more general cases (e.g., 3D models). Besides, their study only considered isotropic random fields. In contrast, Ching and Phoon (2013) considered both isotropic and anisotropic random fields to investigate the influence of element size on the mobilised shear strength, which is defined by the yield stress recorded before FEM fails to converge. They found that when discretizing the random field with a single exponential autocorrelation structure, the element size should be smaller than $0.05\theta_v$ to avoid excessive spatial averaging for an element-level averaging method, and a similar element size requirement also applied for the

mid-point method. Since θ_v is usually small in practice, this requirement would be computationally demanding for RFEM, especially for 3D problems where the requirement may not be realistic. Although the element size adopted in this study is larger than $0.05\theta_v$, Ching and Phoon (2013) described that in such cases, the mid-point method leads to conservative results (smaller values) of mobilized shear strength when assigning shear strengths to elements, while the element-level averaging method would produce unconservative estimates with higher shear strengths than reality. Therefore, the mid-point method is suggested for engineering practice.

In the RFEM analyses of this study, the base of the model is fully fixed, and the back face is prevented to move in the *x*-direction using roller boundaries. For the two end sections along the *y*-direction, the following three types of boundary settings are usually adopted (Chugh 2003; Shen and Karakus 2014): (1) smooth boundary preventing movement in the y – direction. This is adopted when there is no side shear resistance at the boundary; (2) preventing the movement in the x and y directions, considering side shear resistance; (3) fully fixed boundary preventing the movement in the x, y, and z directions, representing a contact without any movements. Hicks and Spencer (2010) discussed that when smooth boundaries are adopted, the two end conditions would tend to exaggerate the failure zones over a suit of Monte Carlo simulations, and biases would occur in these areas. Therefore, they adopted the boundary condition with movements fixed in the x and y directions. This boundary

197 setting is also adopted in the current study.

198 In this study, the soil is modeled as an elastic-perfectly plastic Tresca material.
199 The undrained shear strength c_u is characterized statistically by a log-normal
200 distribution with the mean and coefficient of variation (*COV*) being 19 kPa and 0.3,
201 respectively. The unit weight, Young's modulus (E) and Poisson's ratio (v) are
202 20 kN/m^3, 100 MPa and 0.3, respectively. For slope stability analysis under undrained
203 conditions, v = 0.5 is more appropriate for total stress analysis. This study considers a
204 combination of E = 100 MPa and v = 0.3, as this was used in many previous studies of
205 probabilistic slope stability analyses (Hicks and Spencer 2010; Hicks et al. 2014; Xiao
206 et al. 2016; Hicks and Li 2018). Indeed, E and v have little influences on the FS
207 results by finite element analysis with the strength reduction method (Griffiths and
208 Lane 1999). For comparison, simulations of a 60-m long slope (θ_h = 12 m) are
209 performed using E = 20 MPa and v = 0.495, and the results for the standard deviation
210 of FS are almost identical to the corresponding cases with E = 100 MPa and v = 0.3,
211 as shown in Fig. 5. Also, the results for the mean FS under the two settings (i.e., E =
212 20 MPa; v = 0.495, and E = 100 MPa; v = 0.3) are almost identical (not shown). In
213 this study, the minor autocorrelation distance is fixed to 1 m, while the major
214 autocorrelation distance varies from {2 m, 12 m, 24 m, 60 m}. The rotational angle of
215 the strata varies from {-30°, -60°, 0°, 30°, 60°, 90°}, where the negative values
216 represent clockwise rotation and the positive rotational angles represent anticlockwise
217 rotation.

A deterministic slope stability analysis is first conducted as a benchmark, using the strength reduction method with a non-convergence criterion (Griffiths and Lane 1999). The undrained shear strength is set to be the mean value (i.e. c_u = 19 kPa), and the deterministic FS is 1.214 for the 2D model and 1.244 for the 3D model. It is deemed to be reasonable that the FS by 3D analysis is slightly larger than that by 2D analysis, due to additional constraints imposed by the boundary conditions in the 3D model.

Results

Statistical characteristics of FS

Figs. 5 and 6 show the standard deviation and mean of FS for various scenarios of strata rotation. Considering the rotation around the x and z axes, the statistical characteristics of FS tend to be symmetrical about α = 0°. This is expected, as the same angles with opposite directions of rotation would lead to scenarios that are mirror images of each other, around the plane parallel to the slope cross-section (Figs. 7(a) and (b)). Besides, Figs. 6(a) and (c) show that the mean of FS decreases with larger major autocorrelation distance, for rotated anisotropy around the x and z axes (except with α = 90º around the z axis, which is equivalent to α = 90º around the y axis, and α = 0º around the x axis, which indicates horizontal transverse anisotropy). This phenomenon can be explained by the influence of θ_h on the failure mechanism, which will be discussed in later sections.

For rotated anisotropy around the y axis, a maximum value of the standard deviation (Fig. 5) and a minimum value of the mean FS (Fig. 6(b)) can be observed for all θ_h when the rotational angle is 30°. This indicates that the critical angle of rotation would be around 30^o, considering the slope angle of 45^o in this study. In contrast, the negative angles of rotation would lead to a smaller standard deviation and a higher mean FS, which correspond to lower risk levels. For dip slopes with positive angles of rotation around the y axis, failure through a weak zone occurs more easily (compared to cross-dip or reverse-dip slopes) since it would pass through fewer bedding planes, or only one bedding plane in some cases. Therefore, a dip slope generally constitutes an adverse condition for slope stability. This is also consistent with the observations of Zhu et al. (2019), from their 2D probabilistic slope stability analyses.

When θ_h = 1.5 m and 2 m, the means and standard deviations of FS show small differences at various rotation angles and among the three scenarios of rotated transverse anisotropy. With a small value of θ_h, a continuous weak zone is more difficult to develop, and the potential failure surface would pass through both weak and strong zones alike. Therefore, there would be significant averaging effects on the soil property over the large 3D failure surface, and the average c_u over the failure surface would be close to the mean value over the entire soil mass (i.e., 19 kPa in this study). Consequently, there are smaller dispersions of FS estimates, with the 3D probabilistic results approaching those of the deterministic analyses. In addition, when

the value of θ_h approaches θ_v (i.e., 1 m), the spatially variability pattern becomes similar to the isotropic pattern, and this is also reflected in the trends of the statistics of FS as θ_h decreases (Figs. 5 and 6). This explains why different scenarios of rotated transverse anisotropy lead to similar results at small values of θ_h. Fig. 6 shows that the means of FS for small θ_h values (i.e., θ_h = 1 m, 1.5 m and 2 m) are slightly below the FS from 3D deterministic analyses, with the differences generally less than 4 %. Despite the averaging of c_u over the failure surface, the sliding mass would still pass through the weakest path in each realization of the probabilistic analyses, leading to lower FS values than deterministic estimates. Similar phenomena are also observed in various probabilistic assessments of geotechnical systems (e.g., Cho 2010; Kasama and Whittle 2011; Xiao et al. 2016).

Reliability index

This section investigates the influences of the major autocorrelation distance and the length of the slope model on the results of reliability assessments, through the reliability index (β). The 3D results are also compared with those by 2D probabilistic analyses, to give insights on the potential limitations of plane strain assumptions. Assuming the evaluated FS are normally distributed, the reliability index is given by:

$$\beta = \frac{\mathrm{E(FS)} - 1}{\sigma(\mathrm{FS})} \tag{7a}$$

If FS is assumed to be log-normally distributed, the reliability index is given by

278 (7b)
$$\beta = \frac{\ln\left[\frac{E(FS)}{\sqrt{1+V(FS)^2}}\right]}{\sqrt{\ln[1+V(FS)^2]}}$$

279 where E(FS) = mean of factor of safety; σ(FS) = standard deviation of factor of safety;
280 and V(FS]) = σ(FS) / E(FS).

281 *Effects of major autocorrelation distance*

282 Since the undrained shear strength is the only parameter modeled as random
283 variable, and is assumed to be log-normally distributed, Eq. (7b) is used in the
284 subsequent sections to estimate the reliability index. As the *COV* of FS is not large,
285 the reliability indices estimated by Eqs. (7a) and (7b) are almost identical. Fig. 8(a)
286 shows the reliability index versus various rotational angles when θ_h = 2 m, and the
287 values of β are found to be very high (β > 6) in the 3D analyses for all scenarios of
288 rotated transverse anisotropy. When β > 5, the corresponding probability of failure is
289 below 3×10^{-7}, and the expected performance level of a structure could be defined as
290 "High", according to the U.S. Army Corps of Engineers (1997). This echoes the
291 previous discussions that 3D probabilistic slope stability analyses would resemble
292 deterministic analyses when θ_h and θ_v are small enough, and with the deterministic FS
293 exceeding 1.2, there is a very small chance of slope failure. In contrast, the β values
294 estimated by 2D probabilistic slope stability analyses are much smaller. For both 2D
295 and 3D slope model geometries, failure through a weak zone is difficult to develop
296 when the spatial autocorrelation distances are small, as the soil properties vary rapidly

297 among adjacent elements. Such averaging effects are more pronounced within the
298 failure surface of a 3D slope geometry, compared to that of the corresponding 2D
299 cross-section, since the 3D rupture surface involves a much larger area (arising from
300 the additional dimension) than the 2D slip line. Hence, when θ_h is small, the response
301 of 3D probabilistic slope stability analysis is similar to that by deterministic analysis.

302 Fig. 8 also shows that when $\theta_h \geq 12$ m, with a consideration of rotated anisotropy
303 around the *x* and *z* axes, two slopes entail similar β values when the same degrees of
304 strata rotation are involved in opposite rotational directions (i.e. symmetrical about α
305 = 0º). For rotated anisotropy around the *y* axis, the results of β using 3D probabilistic
306 slope stability analyses approach the corresponding 2D probabilistic analysis results
307 when θ_h is large. This is because when θ_h is large, the soil strata would appear as a
308 continuous layer. Considering rotated anisotropy around the *y* axis, slope failures tend
309 to occur along the entire slope length (*y*-direction) through weak layers, and therefore
310 become similar to those by 2D probabilistic slope stability analyses (Hicks and
311 Spencer 2010) (i.e., failure mode 3). In contrast, considering rotated anisotropy
312 around the *x* and *z* axes, the β values estimated by 3D probabilistic slope stability
313 analyses are significantly larger than those by 2D analyses, showing no tendency to
314 approach the 2D results even with large θ_h values.

315 In practice, the cross-dip slope (Fig. 1(a)) and reverse-dip slope (Fig. 1(c)) are
316 generally favorable scenarios in slope stability assessment, while the dip slope (Fig.
317 1(b)) constitutes an adverse condition. Fig. 9 also shows that the reliability indices for

318 dip slopes are smaller than those in reverse-dip and cross-dip slopes. Meanwhile, it
319 can be seen from Fig. 8 that when $\theta_h \geq 12$ m, for a given α, the reliability of a
320 cross-dip slope is higher than those of a dip slope and a reverse-dip slope. Also, for
321 most of the cases shown in Fig. 9, at a given θ_h, cross-dip slopes generally have a
322 higher reliability than reverse-dip slopes. It should be noted that only the cases with θ_h
323 $\geqslant$ 12 m are included in comparisons of reliability among various slope scenarios in
324 Fig. 9. This is because with very small θ_h values (≤ 2 m), the layering effects are not
325 pronounced in the soil profiles.

326 *Effects of slope length*

327 In 3D probabilistic slope stability analysis considering isotropy and horizontal
328 transverse anisotropy in soil variability, slope reliability was found to be sensitive to
329 the length of the slope model (in the y-direction). Generally, the increase of slope
330 length would lead to a reduction in the slope reliability, due to the diminished
331 constraining effects from the boundaries and the increased probability of occurrence
332 of a critical weak zone (Griffiths et al. 2009a; Hicks and Spencer 2010). In the current
333 work, various slope lengths are considered with $\theta_h = 24$ m, as shown in Figs. 10(a)
334 and (b). According to Fig. 10(a), with horizontal soil strata (i.e. $\alpha = 0°$) and rotated
335 anisotropy around the y axis, the reliability index decreases as the slope length
336 increases, and β values from 3D analyses would eventually fall below the results from
337 2D analyses. In contrast, β values estimated by 3D analysis under rotated anisotropy
338 around the x axis are much larger than those by 2D analysis even when the slope

length is large, and the change of β with various slope lengths is more modest.

Length of sliding mass

Fig. 11 illustrates the definition of the length of sliding mass (or slide length), while its mean value can be obtained over a suite of Monte Carlo simulations. In this study, a slide length in each realization is obtained by the total number of elements along the *y*-direction, located in the row immediately above the slope toe, that have an average nodal *x*-displacement exceeding a threshold value. To determine this threshold value, an approach conceptually similar to that by Hicks et al. (2014) is adopted. A 3D slope model is first constructed with homogeneous soil properties (c_u = 19 kPa), and the cross-section at mid-length ($L/2$) is considered in the 3D analyses. Making use of the displacement response at this mid-length cross-section, a relationship (Fig. 12) can be established between a certain displacement δ (expressed as a percentage of the maximum nodal *x*-displacement) and the number of elements (or percentage of elements in that cross-section) with an average nodal *x*-displacement exceeding δ.

Meanwhile, the volume of the sliding mass in this cross-section can be defined as the volume (or area in 2D) of soil above the slip surface. Herein, the slip surface is determined by a polynomial curve fitting the points of maximum plastic strain in each column of the strain contour. In this case, as shown in Fig. 13, the volume of the sliding mass is estimated to be 58.9% of the entire mesh volume. According to Fig. 12, this volume corresponds to the value of δ which is 32% of the maximum displacement

360 in the model. This δ value is then treated as the threshold when determining the length
361 of sliding mass.

362 The mean slide lengths estimated by this approach are compared against previous
363 studies by Li et al. (2015b) for horizontally deposited soils, as shown in Table 1. Apart
364 from the homogeneous benchmark model, additional simulations were performed
365 with spatially variable soils for different α values. For these cases, 2D slope models
366 were adopted, since the cross-sections of 3D models at mid-length may not always
367 provide representative information of the slip surface due to the spatially variable soil
368 properties. Using these 2D models with different α values, it was found that the
369 thresholds for various cases were within the range of 31% - 34% of the maximum
370 nodal displacement. This means that in general, adopting the calibrated threshold
371 value (32%) would not affect the trends of slide length variations under different α.

372 Under horizontal transverse anisotropy, Hicks et al. (2014) proposed that when θ_h
373 is large relative to the slope height H, the mean of slide length is positively correlated
374 to θ_h. This is because in this case, a sliding mass is attracted to a pocket of weak soils,
375 and a large value of θ_h usually indicates a larger extent of a weak zone (Griffiths et al.
376 2009a). In this study, the mean estimates of slide length and influences of θ_h and α are
377 investigated under rotated transverse anisotropy.

378 Figs. 14(a), (b), and (c) show the mean estimates of slide length with various
379 rotational angles under rotated anisotropy around the x, y, and z axes, respectively.
380 Similar to the previous results for the reliability indices, under rotated anisotropy

around the x and z axes, the mean slide length is similar for two slopes having the same degrees of strata rotation but in opposite rotational directions. Considering rotated anisotropy around the y axis, the rotation of strata (i.e., $\alpha \neq 0°$) can result in larger mean values for slide length. Fig. 14 also shows the changes in slide lengths with different major autocorrelation distances. It can be seen from Fig. 14(b) that under rotated anisotropy around the y axis, when $\theta_h \geq 12$ m, the mean of slide length increases with larger major autocorrelation distance, which is consistent with the above-mentioned observations for horizontal fabric pattern. A similar pattern is also observed with $\alpha = 0°$ around the x axis (Fig. 14(a)) and $\alpha = 90°$ around the z axis in Fig 14(c). In these cases, the soil variations along the y-direction are controlled by θ_h, and a larger value of θ_h leads to a longer mean slide length. In contrast, when considering other cases of rotated anisotropy around the x and z axes (Figs. 14(a) and (c)), an increase in the major autocorrelation distance would lead to smaller mean estimates of the slide length. In these cases, soil variability along the y-direction is controlled by θ_v. As θ_v is usually too small for a continuous weak zone to develop along the direction of slide length, the formation of a potential sliding mass would be mainly controlled by the cumulative effects of weak paths from all the cross-sections within the sliding mass. In this case, a larger major autocorrelation distance would usually result in the easier formation of the weak path for each cross-section, and hence fewer cross-sections may be involved to form a sliding mass. Consequently, for cases of strata rotation around the x and z axes, the mean value of slide length usually shows a modest decrease as θ_h increases. Moreover, as the formation of a rupture

surface is generally easier with larger θ_h, the reliability of the slope tends to decrease, manifested as lower mean estimates of FS shown in Figs. 6(a) and (c).

Conclusion

This paper investigates the effects of three categories of rotated transverse anisotropy on 3D probabilistic slope stability analyses. Their influences on slope reliability can be summarized as follows:

(1) When the major autocorrelation distance (θ_h) is small compared to the slope dimensions, the potential slip surface would pass through weak and strong elements and it is more difficult for a continuous weak zone to emerge. Consequently, the soil properties, when averaged over a large rupture surface, would approach their mean value. Meanwhile, the spatially variability features also approaches the isotropic pattern, and hence the effects of rotated transverse anisotropy are mitigated.

(2) As θ_h increases, a continuous, or semi-continuous, weak zone of soils can form within a slope. For rotated transverse anisotropy around the x and z axes, the slope reliability revealed by 3D analyses shows no tendency to approach the results by 2D analyses. Besides, under these scenarios, when the major autocorrelation distance increases, the mean value of slide length would slightly decrease. These findings differ from those for horizontal transverse anisotropy reported in previous studies.

(3) For rotated transverse anisotropy around the y axis, the slope reliability by 3D analyses tends to be similar to that in 2D analyses with large values of θ_h. The mean

slide length in this case would increase with the major autocorrelation distance. These observations are similar to those reported in previous studies considering horizontal transverse anisotropy.

(4) Considering rotated transverse anisotropy around the *x* axis, the changes in the slope reliability are relatively insensitive to the length of the slope in the out-of-plane direction. Conversely, the reliability of a slope would reduce considerably with slope length when soils display horizontally deposited fabric pattern or with pronounced rotated anisotropy around *y* axis.

(5) Cross-dip slopes and reverse-dip slopes are usually regarded as favorable features for slope stability. In this study, it is found that in general, cross-dip slopes could be more favorable scenarios for slope reliability, when spatial variability of soil properties in various directions are considered.

Acknowledgments

The present project is funded by the Research Grants Council of the Hong Kong Special Administrative Region (Project No. 15220415).

References

Cheng, Y.M., and Lau, C.K. 2008. Slope stability analysis and stabilization. Routledge, London.

Ching, J.Y., and Phoon, K.K. 2013. Effect of element sizes in random field finite

element simulations of soil shear strength. Computers and Structures, 126: 120-134.

Cho, S.E. 2010. Probabilistic assessment of slope stability that considers the spatial variability of soil properties. Journal of Geotechnical and Geoenvironmental Engineering, 136(7): 975-984.

Chugh, A.K. 2003. On the boundary conditions in slope stability analysis. International Journal for Numerical and Analytical Methods in Geomechanics, 27: 905-926.

Fenton, G.A., and Vanmarcke, E.H. 1990. Simulation of random fields via local average subdivision. Journal of Engineering Mechanics, 116(8): 1733-1749.

Griffiths, D.V., and Fenton, G.A. 2001. Bearing capacity of spatially random soil: the undrained clay Prandtl problem revisited. Geotechnique, 51(4): 351-359.

Griffiths, D.V., and Fenton, G.A. 2004. Probabilistic slope stability analysis by finite elements. Journal of Geotechnical and Geoenvironmental Engineering, 130(5): 507-518.

Griffiths, D.V., Huang, J., and Fenton, G.A. 2009a. On the reliability of earth slopes in three dimensions. Proceeding of the Royal Society A, 465(2110): 3145-3164.

Griffiths, D.V., and Lane, P.A. 1999. Slope stability analysis by finite elements. Geotechnique, 49(3): 387-403.

Griffiths, D.V., and Marquez, R.M. 2007. Three-dimensional slope stability analysis

461 by elasto-plastic finite elements. Geotechnique, 57: 537-546.

462 Griffiths, D.V., Schiermeyer, R.P., Huang, J., and Fenton, G.A. 2009b. Influence of
463 anisotropy and rotation on probabilistic slope stability analysis by RFEM.
464 Proceedings of GeoHalifax, Paper 408, (CD-ROM).

465 Hicks, M.A., and Li, Y. 2018. Influence of length effect on embankment slope
466 reliability in 3D. International Journal for Numerical and Analytical Methods in
467 Geomechanics, 42(1):891-915.

468 Hicks, M.A., Nuttall, J.D., and Chen, J. 2014. Influence of heterogeneity on 3D slope
469 reliability and failure consequence. Computers and Geotechnics, 61(3): 198-208.

470 Hicks, M.A., and Onisiphorou, C. 2005. Stochastic evaluation of static liquefaction in
471 a predominantly dilative sand fill. Geotechnique, 55(2): 123-133.

472 Hicks, M.A., and Spencer, W.A. 2010. Influence of heterogeneity on the reliability
473 and failure of a long 3D slope. Computers and Geotechnics, 37: 948-955.

474 Huang, J., Griffiths, D.V., and Fenton, G.A. 2010. System reliability of slopes by
475 RFEM. Soils and Foundations, 50(3): 343-353.

476 Huang, J., and Griffiths, D.V. 2015. Determining an appropriate finite element size for
477 modelling the strength of undrained random soils. Computers and Geotechnics, 69:
478 506-513.

479 Jha, S.K., and Ching, J.Y. 2013. Simplified reliability method for spatially variable

480 undrained engineered slopes. Soils and Foundations, 53(5): 708-719.

481 Jiang, S.H., and Huang, J.S. 2016. Efficient slope reliability analysis at
482 low-probability levels in spatially variable soils. Computers and Geotechnics, 75:
483 18-27.

484 Jiang, S.H., Li, D.Q., Zhang, L.M., and Zhou, C.B. 2014. Slope reliability analysis
485 considering spatially variable shear strength parameters using a non-intrusive
486 stochastic finite element method. Engineering Geology, 168(1): 120-128.

487 Jiang, S.H., Li, D.Q., Cao, Z.J., Zhou, C.B., and Phoon, K.K. 2015. Efficient system
488 reliability analysis of slope stability in spatially variable soils using Monte Carlo
489 simulation. Journal of Geotechnical and Geoenvironmental Engineering, 141(2):
490 04014096.

491 Kasama, K., and Whittle, A.J. 2011. Bearing capacity of spatially random cohesive
492 soil using numerical limit analyses. Journal of Geotechnical and Geoenvironmental
493 Engineering, 137(11): 989-996.

494 Li, C.C., and Der Kiureghian A. 1993. Optimal discretization of random fields.
495 Journal of Engineering Mechanics, 119(6): 1136-1154.

496 Li, D.Q., Jiang, S.H., Cao, Z.J., Zhou, W., Zhou, C.B., and Zhang, L.M. 2015a. A
497 multiple response-surface method for slope reliability analysis considering spatial
498 variability of soil properties. Engineering Geology, 187: 60-72.

499 Li, Y.J., Hicks, M.A., and Nuttall, J.D. 2015b. Comparative analyses of slope
500 reliability in 3D. Engineering Geology, 196: 12-23.

501 Li, L., and Chu, X.S. 2015. Multiple response surfaces for slope reliability
502 analysis. International Journal for Numerical and Analytical Methods in
503 Geomechanics, 39(2): 175-192.

504 Li, L., Wang, Y., Cao, Z.J., and Chu, X.S. 2013. Risk de-aggregation and system
505 reliability analysis of slope stability using representative slip surfaces. Computers and
506 Geotechnics, 53(3): 95-105.

507 Li, Y.J., Hicks, M.A., and Vardon, P.J. 2016. Uncertainty reduction and sampling
508 efficiency in slope designs using 3D conditional random fields. Computers and
509 Geotechnics, 79: 159-172.

510 Liu, L.L., Deng, Z.P., Zhang, S.H., and Cheng, Y.M. 2018. Simplified framework for
511 system reliability analysis of slopes in spatially variable soils. Engineering Geology,
512 239: 330-343.

513 Liu, W.F., and Leung, Y.F. 2018. Characterising three-dimensional anisotropic spatial
514 correlation of soil properties through in situ test results. Geotechnique, 69(9):
515 805-819.

516 Lo, M.K. and Leung, Y.F. 2017. Probabilistic analyses of slopes and footings with
517 spatially variable soils considering cross-correlation and conditioned random field.
518 Journal of Geotechnical and Geoenvironmental Engineering, 143(9): 04017044.

519 Lo, M.K. and Leung, Y.F. 2018. Reliability assessment of slopes considering sampling
520 influence and spatial variability by Sobol' sensitivity index. Journal of Geotechnical
521 and Geoenvironmental Engineering, 144(4): 04018010.

522 Shen, J.Y., and Karakus, M. 2014. Three-dimensional numerical analysis for rock
523 slope stability using shear strength reduction method. Canadian Geotechnical Journal,
524 51: 164-172.

525 U.S. Army Corps of Engineers. 1997. Engineering and design: introduction to
526 probability and reliability methods for use in geotechnical engineering. Department of
527 the Army, Washington. D.C. Engineer Technical Letter, 1110-2-547.

528 Vanmarcke, E.H. 1984. Random fields: Analysis and synthesis. MIT Press,
529 Cambridge MA.

530 Varkey, D., Hicks, M.A., and Vardon, P.J. 2019. An improved semi-analytical method
531 for 3D slope reliability assessments. Computers and Geotechnics, 111: 181-190.

532 Wang Y., Cao Z.J., and Au, S.K. 2011. Practical reliability analysis of slope stability
533 by advanced Monte Carlo simulations in a spreadsheet. Canadian Geotechnical
534 Journal, 48(1): 162-172.

535 Xiao, T., Li, D.Q., Cao, Z.J., Au, S.K., and Phoon, K.K. 2016. Three-dimensional
536 slope reliability and risk assessment using auxiliary random finite element method.
537 Computers and Geotechnics, 79: 146-158.

538 Zhu, H., and Zhang, L.M. 2013. Characterizing geotechnical anisotropic spatial
539 variations using random field theory. Canadian Geotechnical Journal, 50:723-734.

540 Zhu, H., Zhang, L.M., and Xiao, T. 2019. Evaluating the stability of anisotropically
541 deposited soil slopes. Canadian Geotechnical Journal, 56: 753-760.

List of symbols

c_u	Undrained shear strength
e	Residual of soil properties in spatially variable soils
E(FS)	Mean of FS
FS	Factor of safety
H	Slope height
L	Slope length
L	Cholesky factor of **R**
n_e	Number of elements of random field
R	Autocorrelation matrix
s	Independent standard normal random vector
u	Deterministic trend of spatially variable soil properties
V	Covariance matrix
z	Vector of spatially variable soil properties
α	Dip angle of strata
β	Reliability index
Δ_x	Separation distance between two locations in x-direction
Δ_y	Separation distance between two locations in y-direction
Δ_z	Separation distance between two locations in z-direction
ε	Standard Gaussian random field

θ_h	Major autocorrelation distance
θ_v	Minor autocorrelation distance
$\mu_{\ln z}$	Mean of the logarithm of soil property
ρ	Correlation coefficient
σ^2	Variance
σ(FS)	Standard deviation of FS
$\sigma_{\ln z}$	Standard deviation of the logarithm of soil property

List of Tables

Table 1 Comparison of mean slide lengths of slopes with horizontally deposited soils under undrained conditions with θ_v = 1 m.

List of Figures

Table 1 Comparison of mean slide lengths of slopes with horizontally deposited soils under undrained conditions with θ_v = 1 m.

θ_h (m)	Current study of a 60-m slope (% of total slope length)	Li et al. (2015b) of a 50-m slope (% of total slope length)
2	60.84	Around 60
12	38.97	Around 38
24	41.7	Around 40

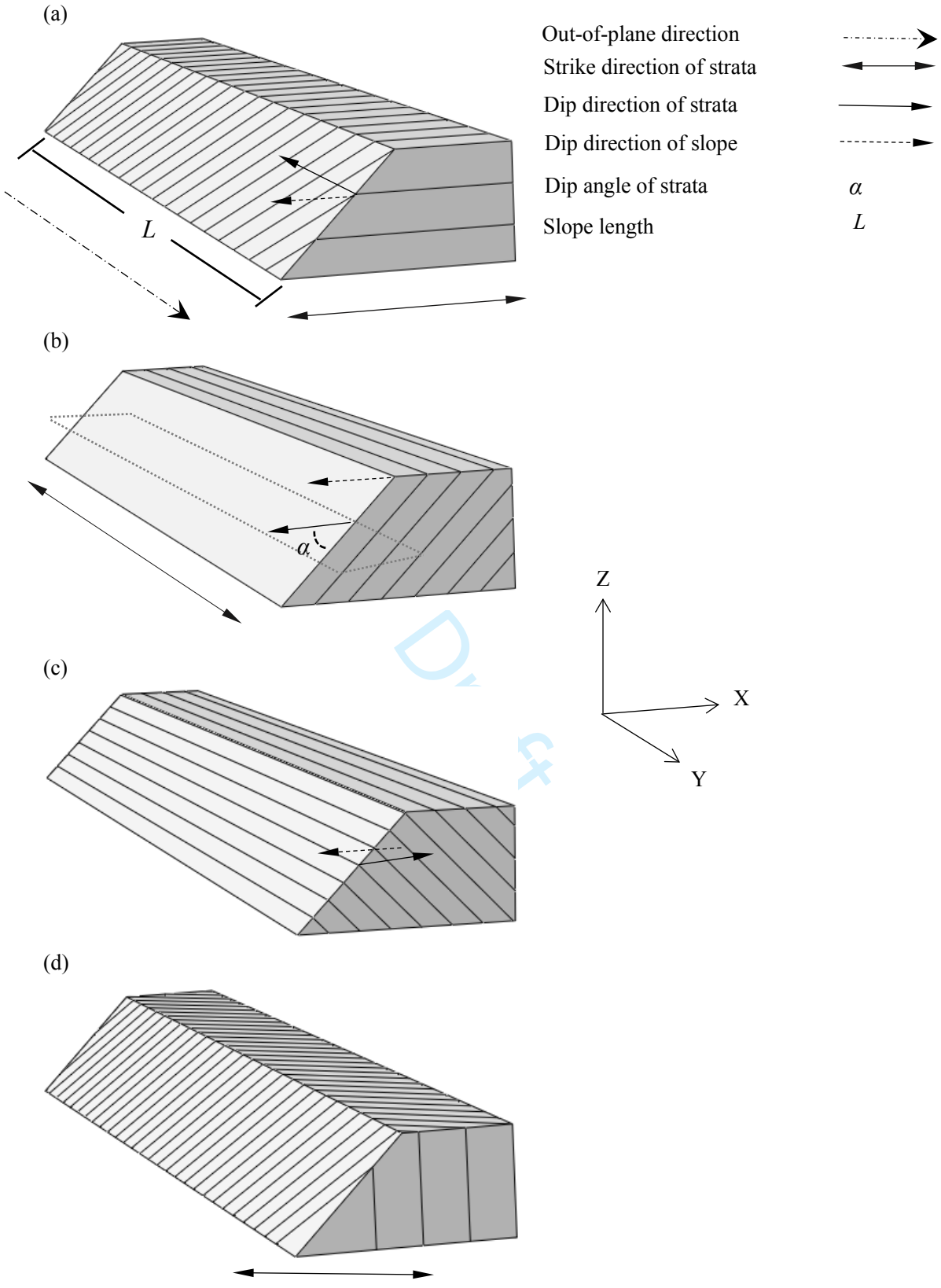

Fig. 1 (a) Strata rotating around *x* axis (cross-dip slope); (b) strata rotating around *y* axis (dip slope); (c) strata rotating around *y* axis (reverse-dip slope); (d) strata rotating around *z* axis.

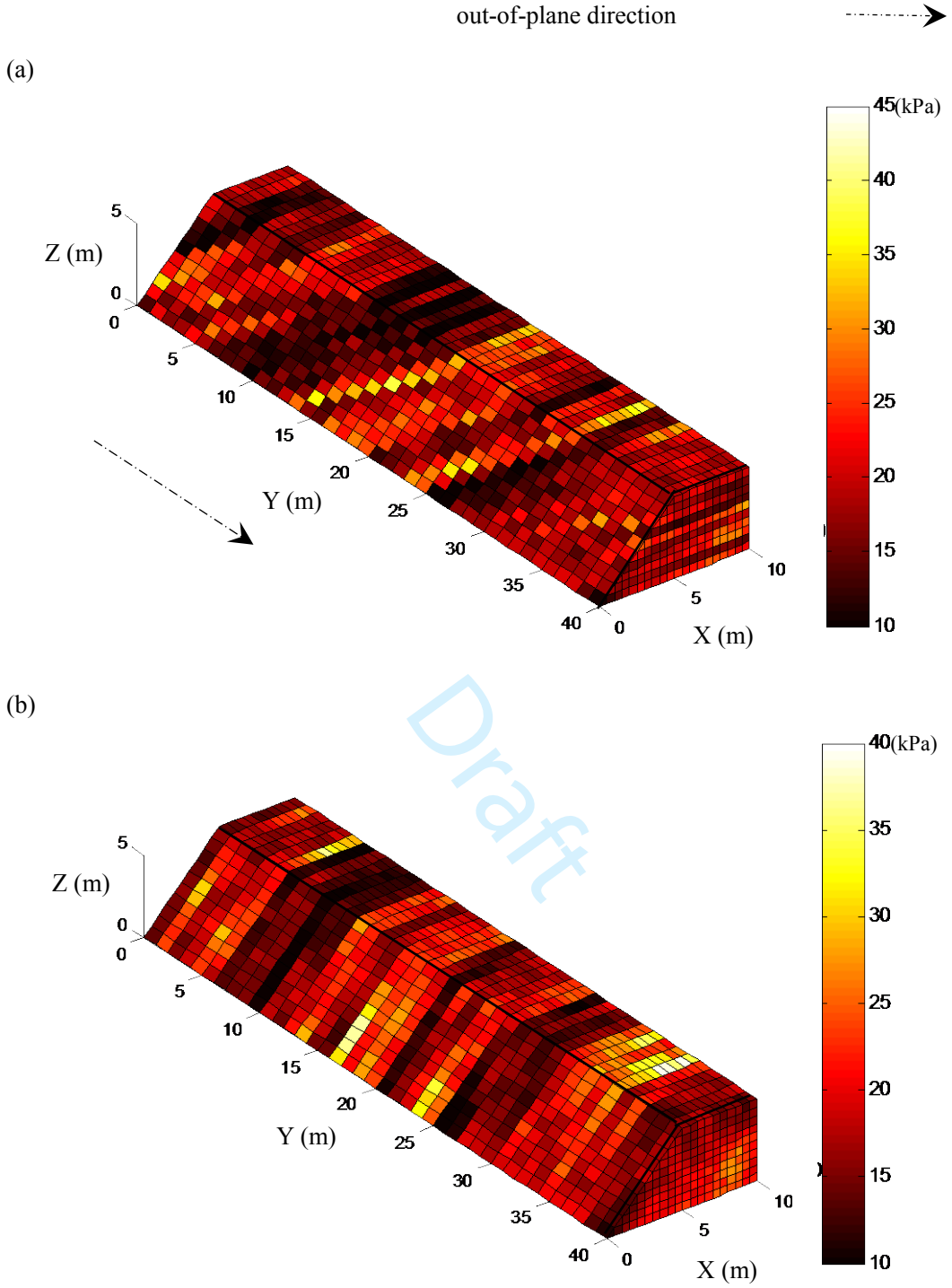

Fig. 2 Typical realizations of random fields of undrained shear strength under rotation around x axis: (a) $\alpha = 30°$; (b) $\alpha = 90°$.

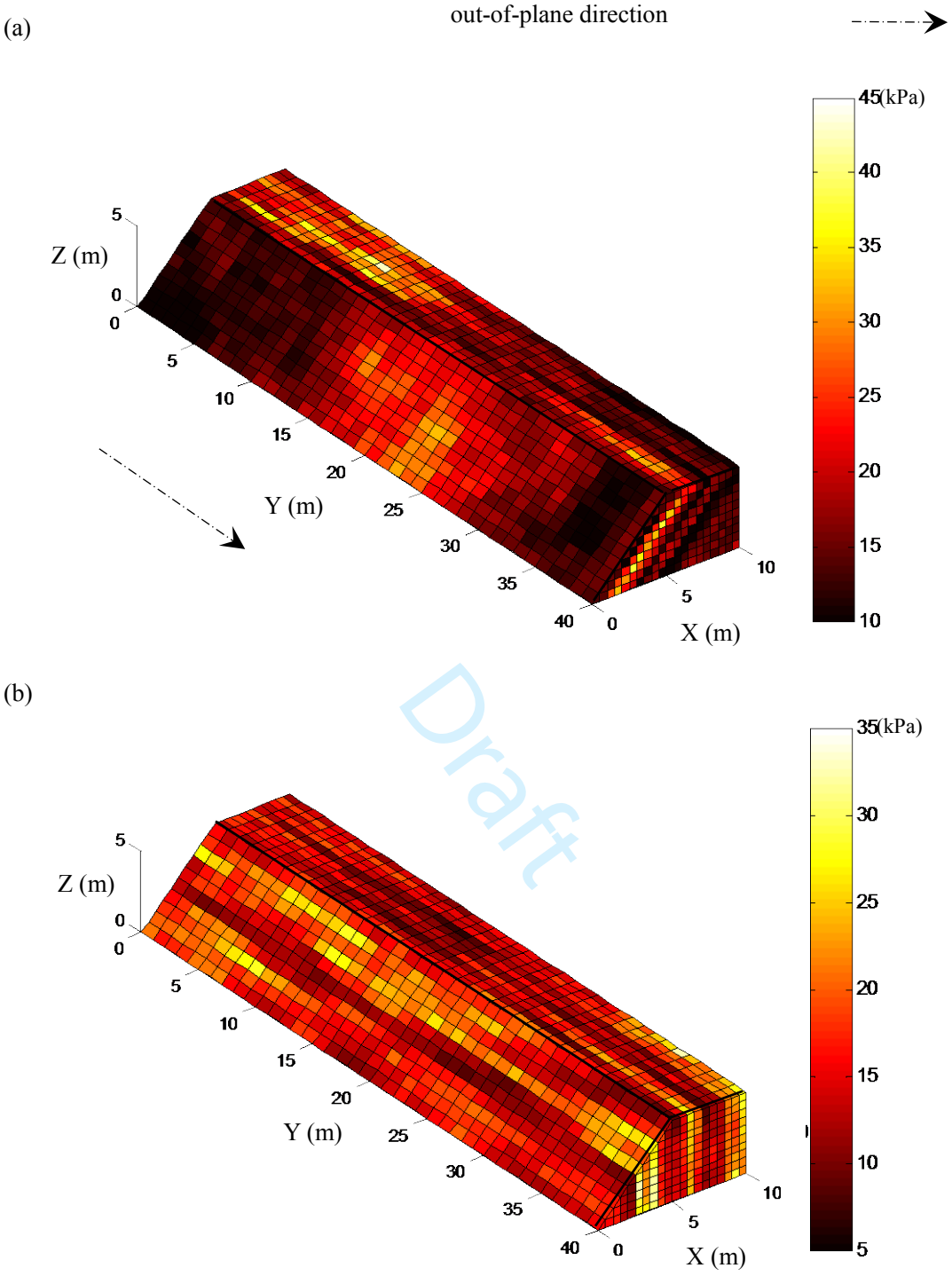

Fig. 3 Typical realizations of random fields of undrained shear strength under rotation around y axis: (a) $\alpha = 45°$; (b) $\alpha = 90°$.

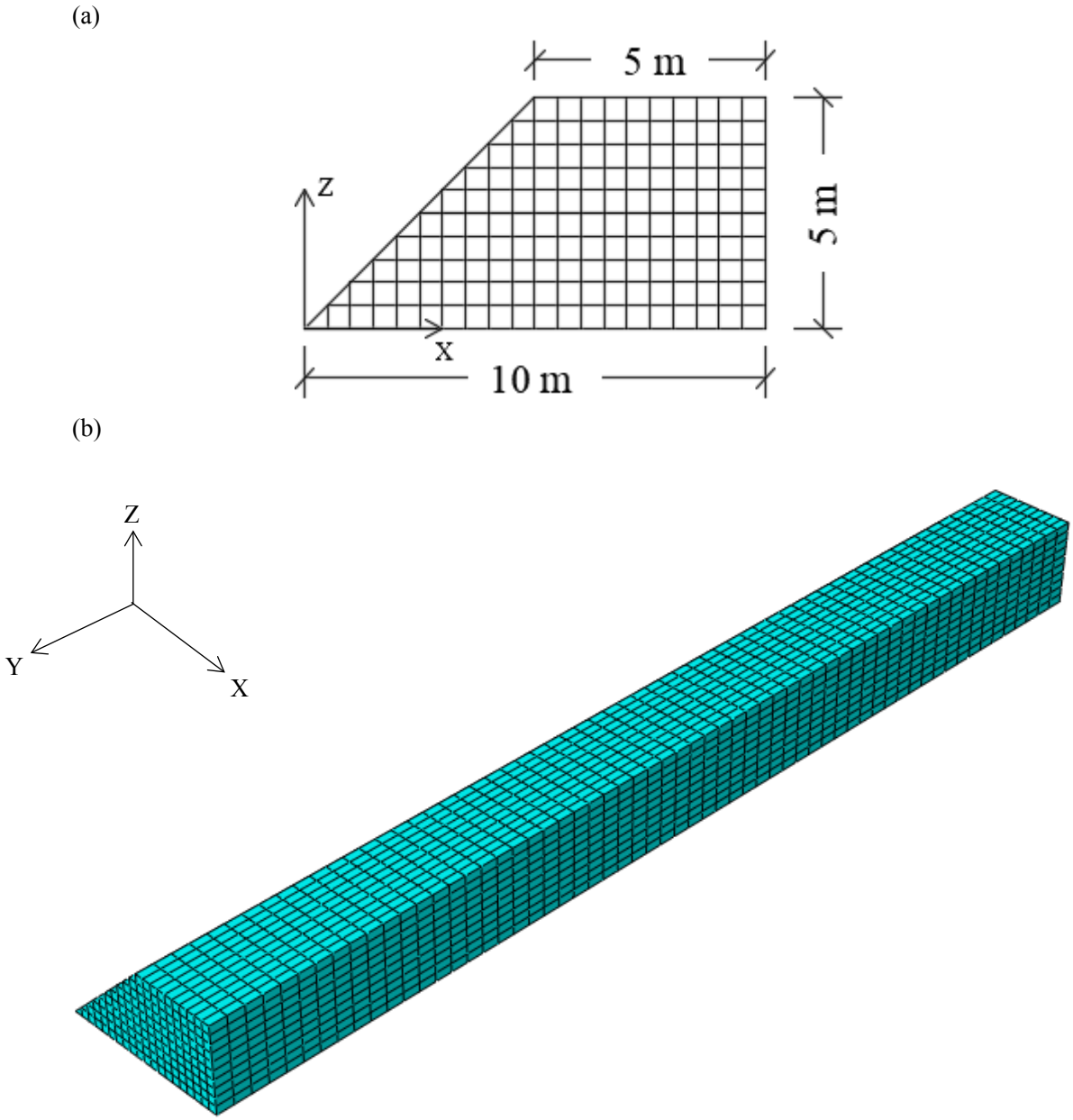

Fig. 4 Slope geometry and finite element mesh: (a) cross-section through mesh; (b) finite element mesh for a 3D slope.

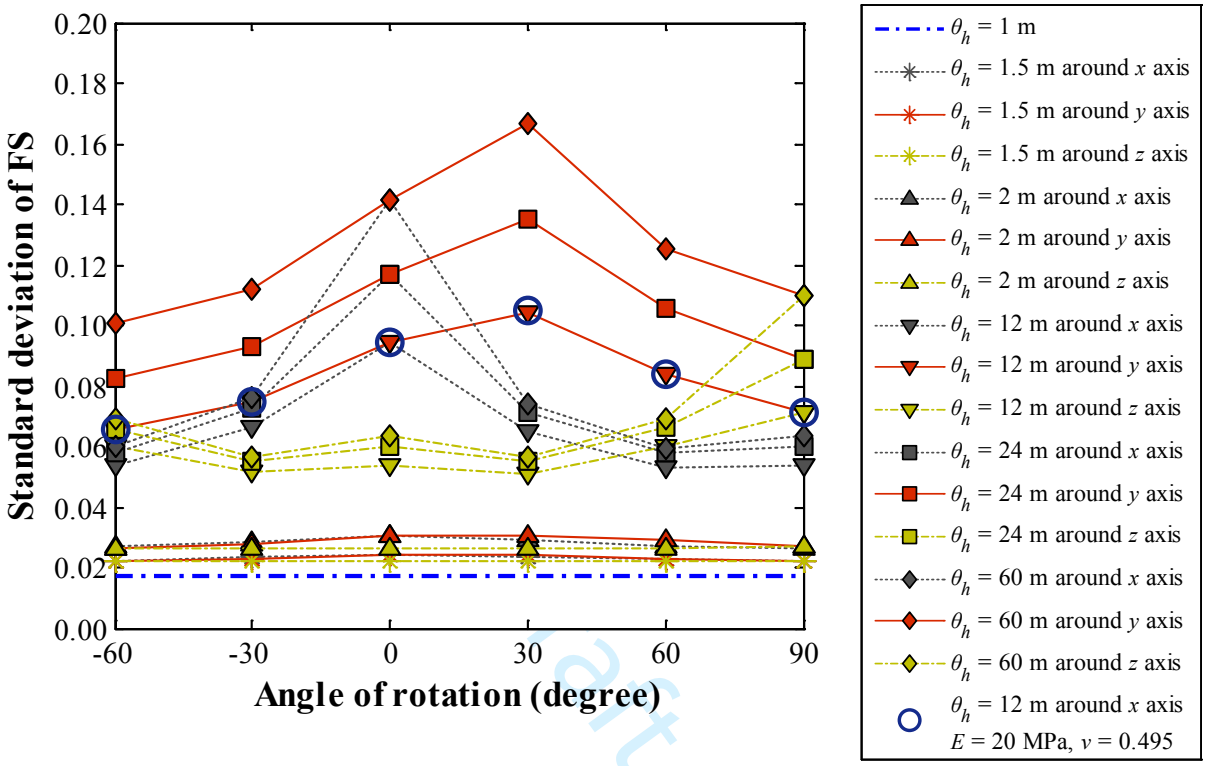

Fig. 5 Standard deviation of FS versus angle of rotation.

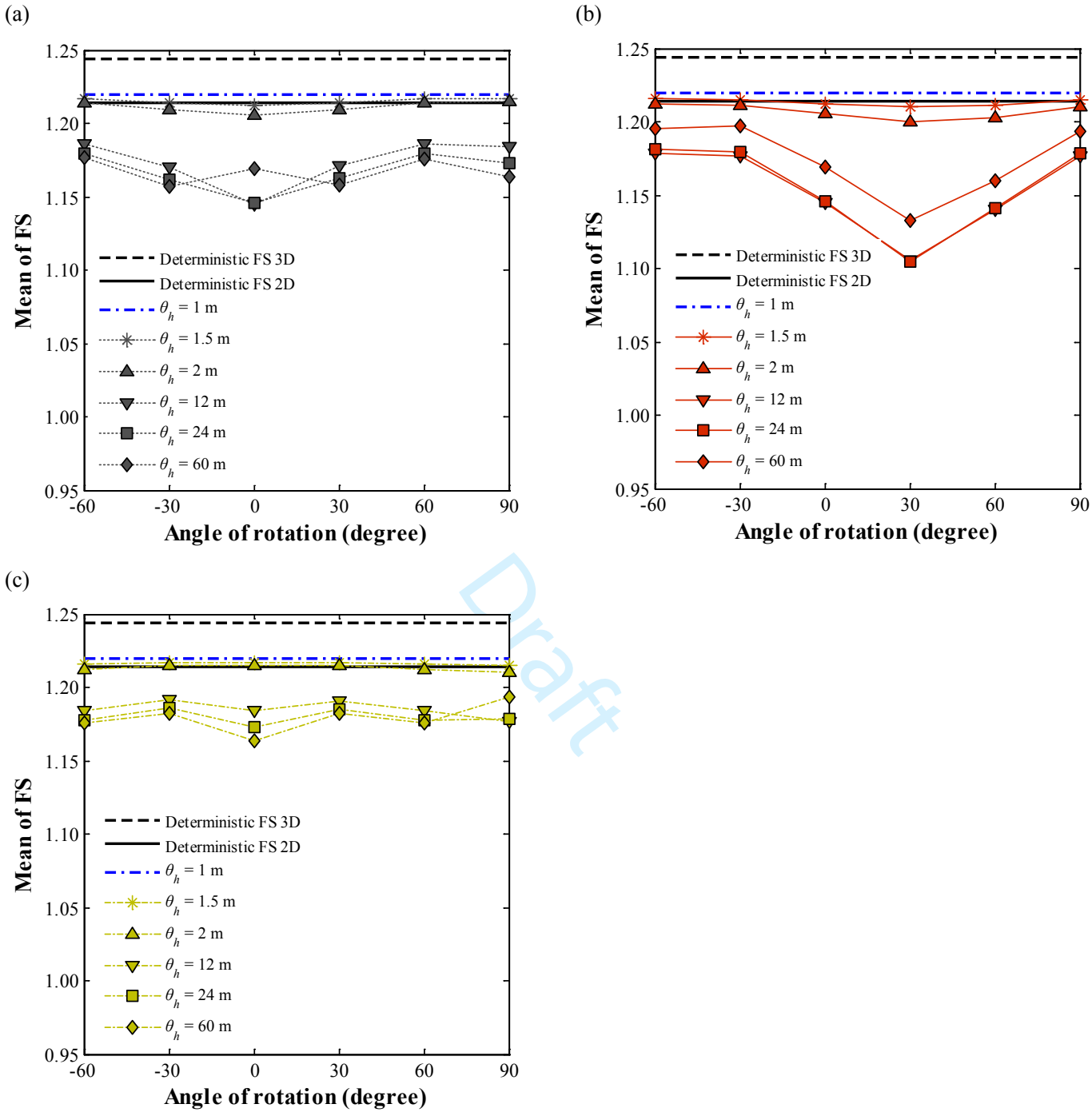

Fig. 6 Mean of FS versus angle of rotation under: (a) rotated anisotropy around *x* axis; (b) rotated anisotropy around *y* axis; (c) rotated anisotropy around *z* axis.

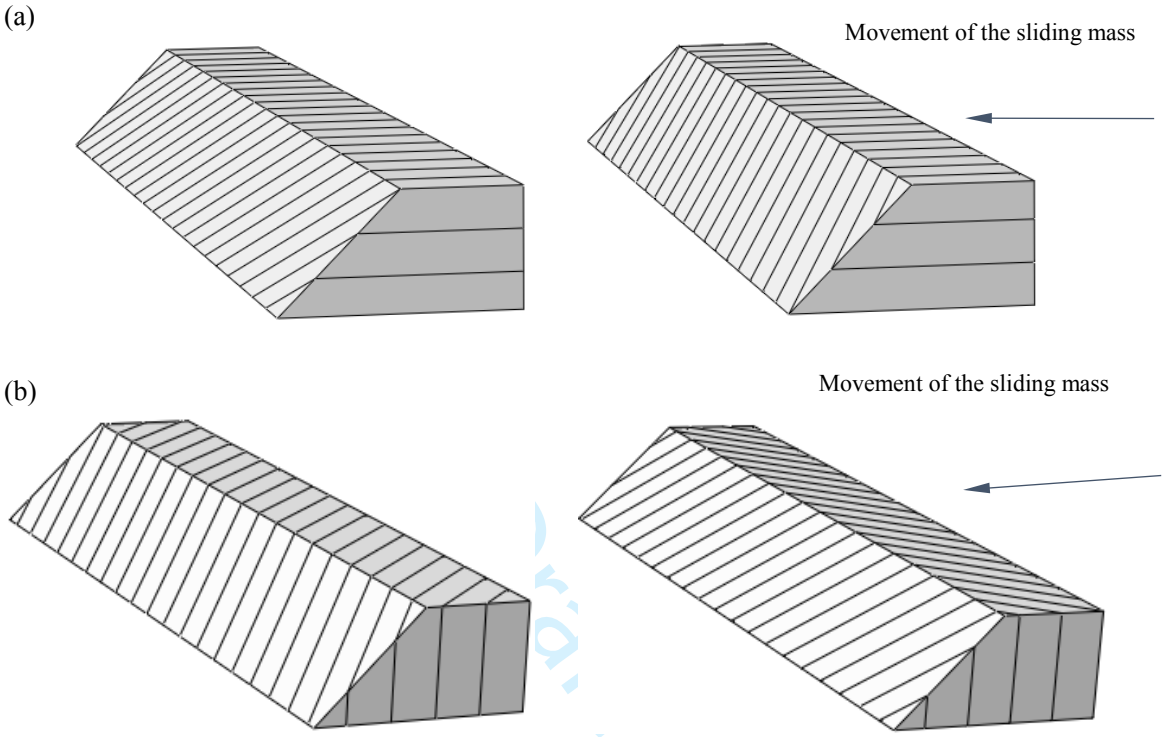

Fig. 7 (a) Two slopes under rotated anisotropy around *x* axis with the same degrees of rotation and opposite rotational directions; (b) two slopes under rotated anisotropy around *z* axis with the same degrees of rotation and opposite rotational directions.

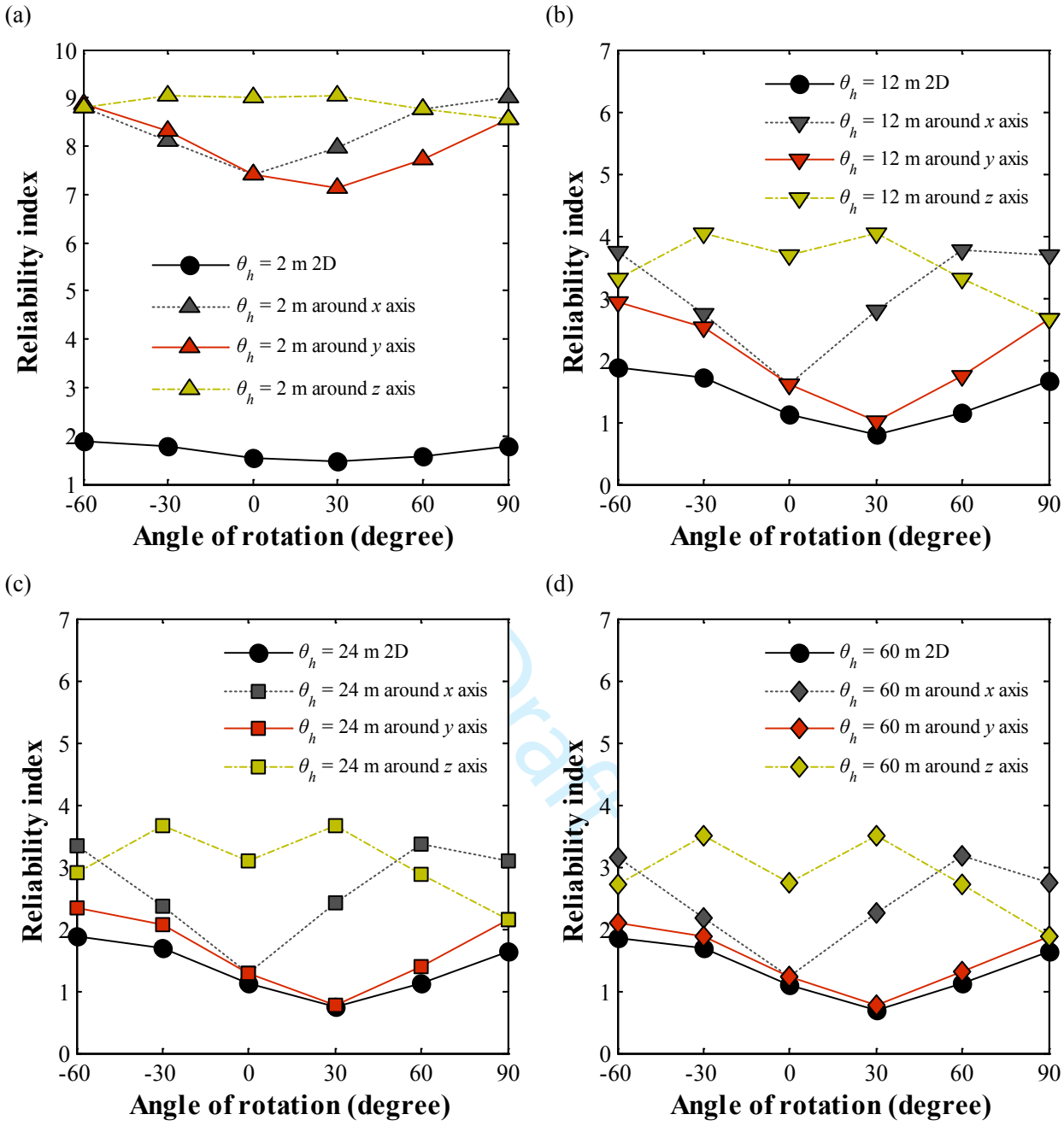

Fig. 8 Reliability index β by Eq. (7b) versus angle of rotation : (a) θ_h = 2 m; (b) θ_h = 12 m; (c) θ_h = 24 m; (d) θ_h = 60 m.

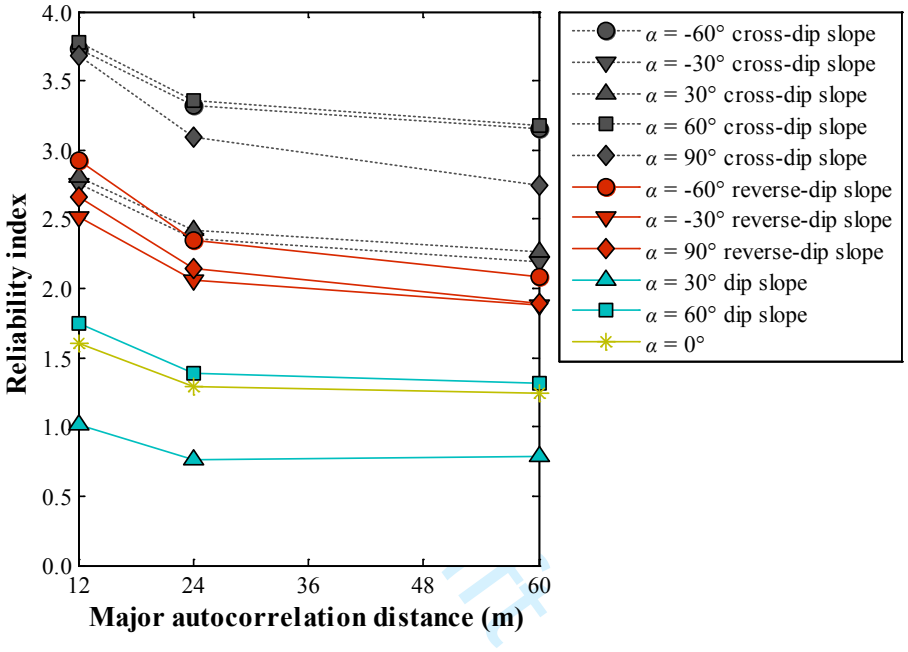

Fig. 9 Reliability index β by Eq. (7b) versus major autocorrelation distance.

(a)

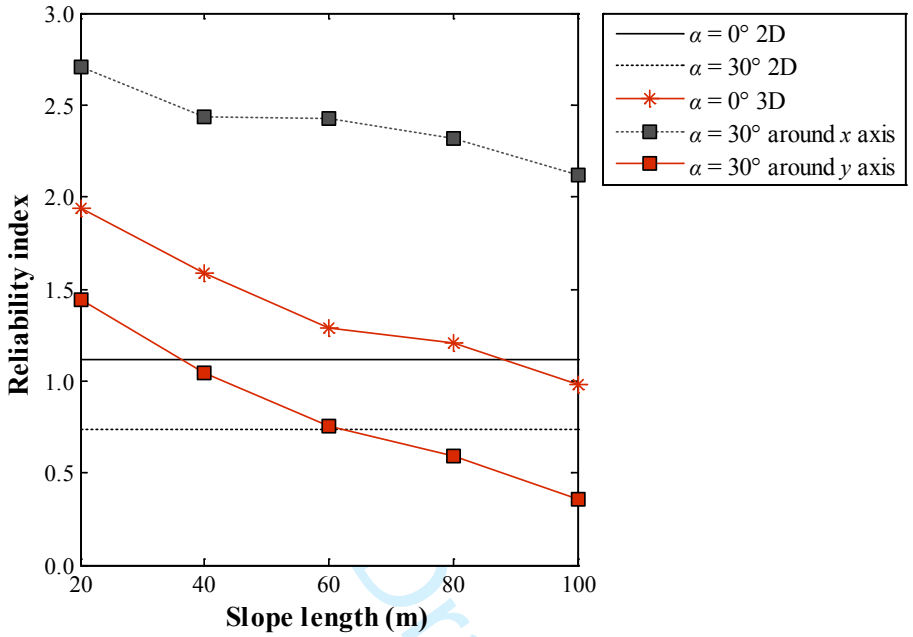

(b)

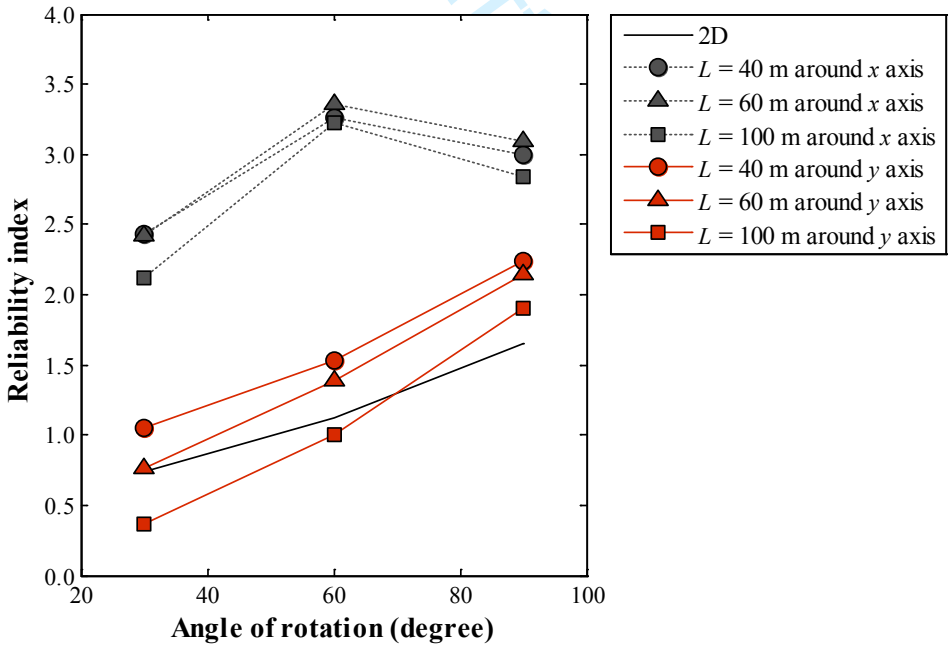

Fig. 10 Reliability index β by Eq. (7b) with θ_h = 24 m versus: (a) slope length; (b) angle of rotation.

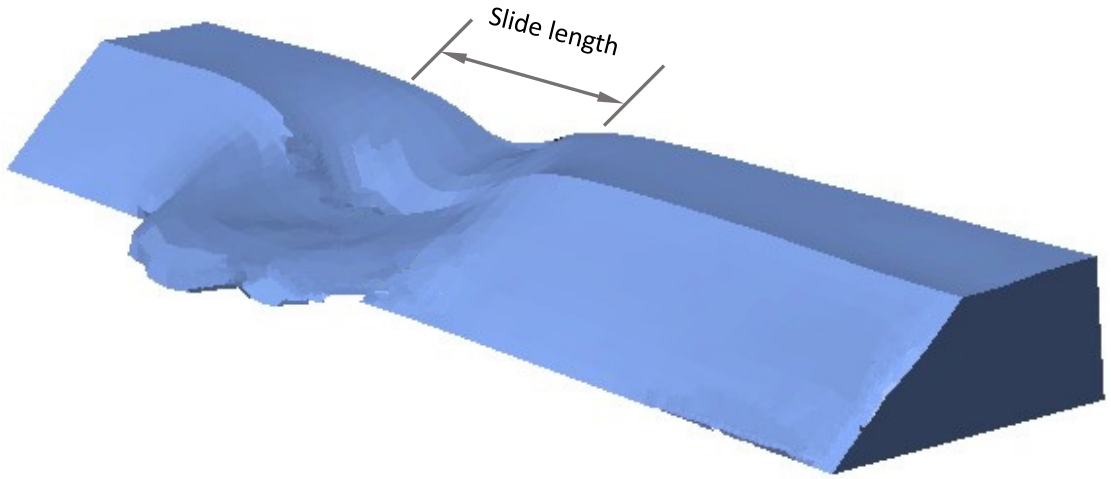

Fig. 11 Slide length of a slope.

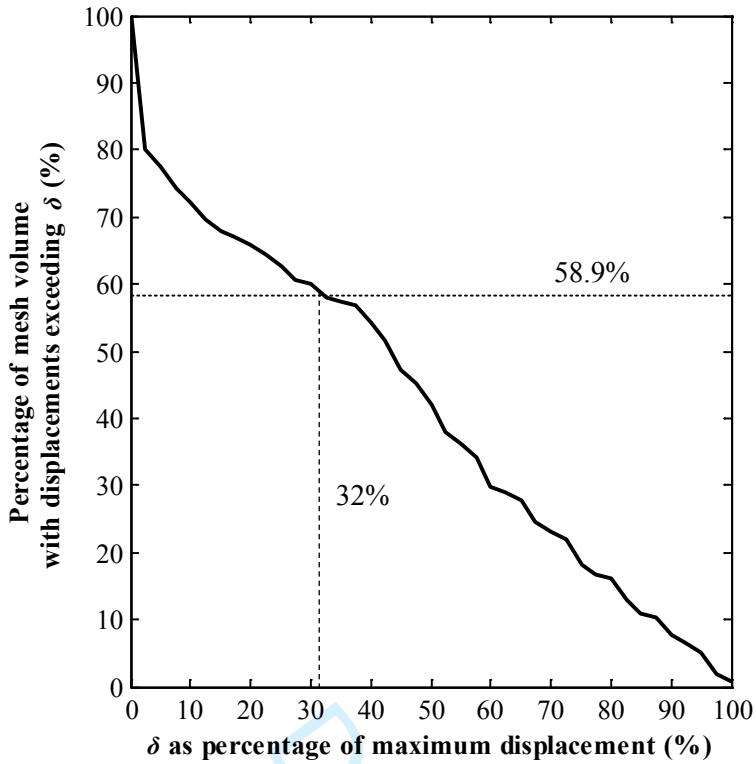

Fig. 12 Relationship between displacement δ and the volume of soil mass with displacements exceeding δ.

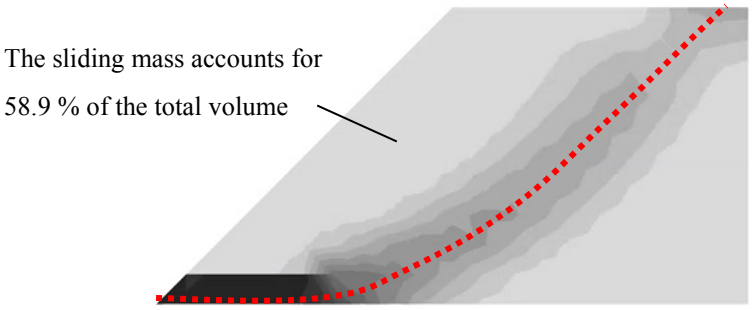

Fig. 13 Slip surface and plastic strain contour (darker zones indicate higher shear strain).

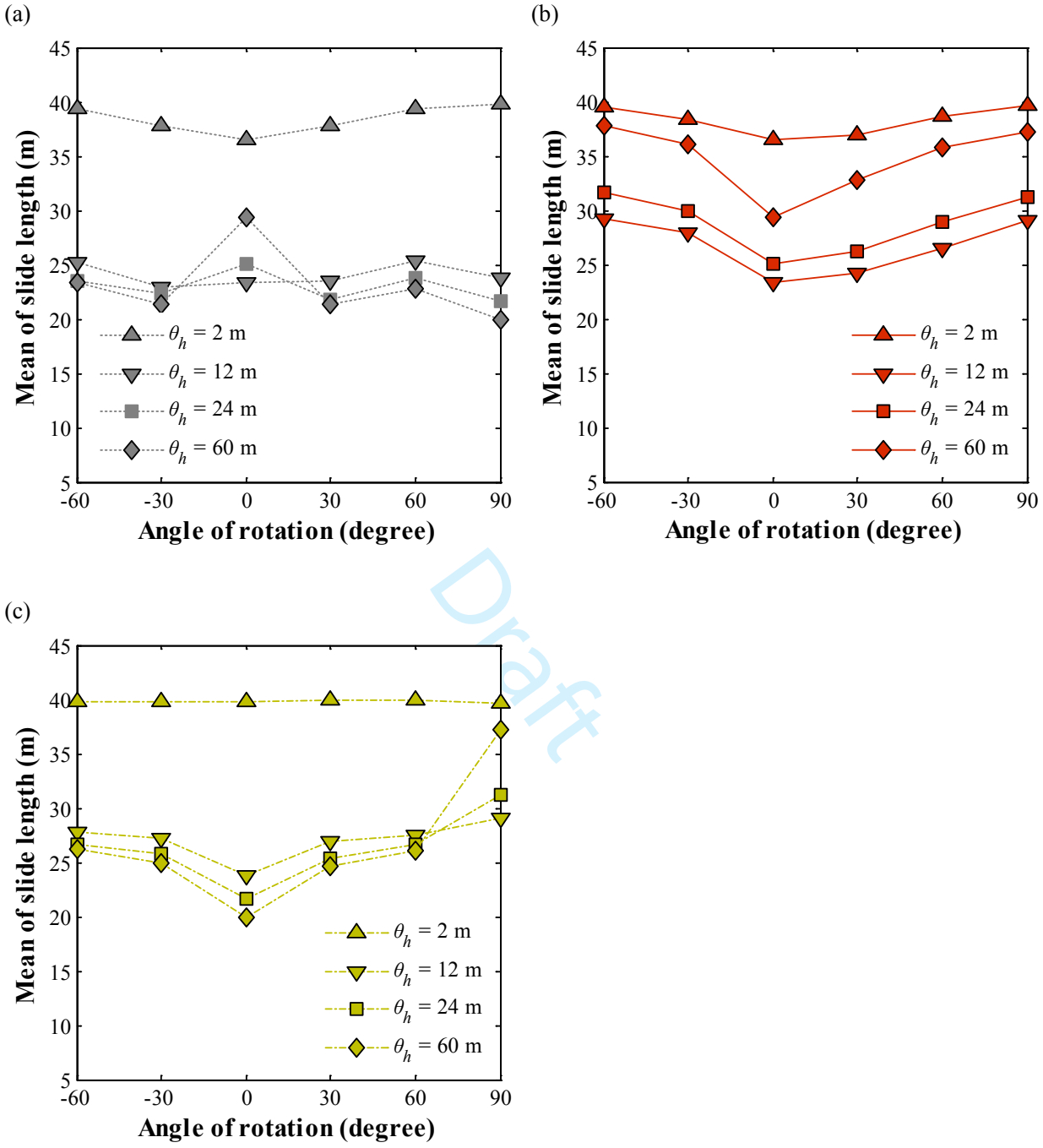

Fig. 14 Mean of slide length versus angle of rotation considering the threshold of 32 % of the maximum computed displacement: (a) rotated anisotropy around *x* axis; (b) rotated anisotropy around *y* axis; (c) rotated anisotropy around *z* axis.